2-D Hypersonic Non-equilibrium Flow Simulation using r-p Adaptive Time-Implicit Discontinuous Galerkin Method

Journal:	*51st Aerospace Sciences Meeting*
Manuscript ID:	Draft
luMeetingID:	1965
Date Submitted by the Author:	n/a
Contact Author:	Bhatia, Ankush

2-D Hypersonic Non-equilibrium Flow Simulation using r-p Adaptive Time-Implicit Discontinuous Galerkin Method

Ankush Bhatia[1] and Subrata Roy[2]
Applied Physics Research Group, Department of Mechanical and Aerospace Engineering, University of Florida, Gainesville, FL – 32611, USA

We apply r-p adaptive time-implicit Discontinuous Galerkin (DG) methods to 2-D hypersonic flow problems. Previous applications of DG method were limited to viscous hypersonic flows. Here we extend DG to chemically reacting hypersonic flows with thermal non-equilibrium. Use of p-adaptive method, allows us to interpolate non-smooth shock region with piecewise element-averaged polynomial (p = 0) and with higher order polynomials (p ≥ 1) where the flow features are mathematically smooth. Also by redistributing (r) elements in critical regions about shock, we get accurate solutions without employing excessive mesh elements (h). Specifically we study the flow over a stationary cylinder using (i) inviscid, (ii) viscous, and (iii) thermo-chemical non-equilibrium flow regimes. We compare our simulations with published results.

Nomenclature

E	=	total energy
e_v	=	vibrational energy
F	=	inviscid flux vector
F_v	=	viscous flux vector
h	=	enthalpy
P	=	pressure
q''	=	heat flux
ρ	=	density
S	=	source vector
T	=	translational-rotational temperature
T_v	=	vibrational temperature
τ	=	shear stress
u	=	x-velocity
U	=	solution vector
v	=	y-velocity
ω	=	production rate
x	=	spatial coordinate

I. Introduction

DISCONTINUOUS Galerkin (DG) methods[1-5] have been widely used for problems like compressible and incompressible flows, shallow water flows and flow through porous media, gas dynamics and magnetohydrodynamics. They have many favorable properties like low diffusion/dispersion, local mass conservation, and easy h-p adaption implementation due to localized approximation spaces. Given such properties of DG methods, we want to implement them for problems like thermal ablation, chemically reacting flows and eventually plasma dynamics problems.

DG methods also have several advantages of being a high-order accurate method[6, 7], being able to deal with complex shaped geometries using unstructured grid without much increasing the code complexity. For implicit time integration, this method results in an element wise block structure of the jacobian matrix, without any overlap of local matrices of the

[1] Graduate student, student member, AIAA
[2] Associate Professor, Associate Fellow, AIAA

adjacent elements. This makes DG method very suitable for a parallel system[8]. Major disadvantage of this method, though, to date has been high computational cost and large memory requirements (by requirement for large number of degree of freedoms). Efforts have been made to reduce computational costs by preconditioning the implicit matrix[10] or using line solvers or multigrid approaches[8, 9].

High-order accuracy in regime of finite difference and finite volume methods comes by extending the stencil to more and more neighboring elements[6, 7]. This however increases the complexity of the method. To ensure high-order accuracy at the boundary, biased schemes of the same order are needed at boundary and elements close to boundary. This makes the code more prone to stability problems. This problem is easily avoided in DG methods, where order is increased by simply increasing the polynomial accuracy within the elements. This makes DG method more robust, but it adds onto total number of degrees of freedom with any increase in the order of accuracy[11]. Finite difference and finite volume methods do not need increase in number of degrees of freedom for increasing the order of accuracy. By keeping to less number of mesh elements, with increased order of accuracy DG methods can offset this disadvantage, in comparison to FD and FV methods.

Another main difference between finite volume (FV) and DG method, is that even if FV is higher order accurate, the solution is still piecewise constant within the cell, and it will be difficult to capture high gradients especially at a wall without sufficiently large number of cells close to wall. DG method however for $p \geq 1$, enforces the Dirichlet boundary conditions more strictly than FV method or even for DG with $p = 0$ case. Hence the surface properties, like C_f and C_d are more likely to be evaluated correctly with DG method with lesser number of elements. This was actually reported in Ph.D. thesis by Burgess[7], where DG solver for nearly half as computational time as FV (both methods being 2nd order accurate), attained 39% reduction in the computed drag error. It is surmised therefore that DG method may need lesser number of mesh elements for capturing steep solution gradients (at boundary) in comparison to FV method with same high order accuracy.

DG methods have been applied to various problems of industrial interest like aerodynamics flows over aerofoil, Magnetohydrodynamics etc., but its application to more complex and involved problems like thermal ablation, non-equilibrium hypersonic flows and plasma is yet unexplored. We applied DG methods to 1-D thermal ablation problems in our previous work[12]. However its application to a 2-D thermal ablation problem requires us to have a capability to solve 2-D hypersonic flow outside the re-entry vehicle. Therefore in this paper, we focus on application of DG methods to hypersonic flow problems, extending the work that's already done in inviscid and viscous hypersonic[6, 7, 13] flows to hypersonic flows with thermo-chemical non equilibrium. We will also extend our current work to solving 2-D thermal ablation problems with flow outside vehicle in future. Approaches, available in literature have so far focused on using either slope limiters[15] or artificial dissipation[7, 14] to capture shocks especially for hypersonic flows. An approach to capture shocks without a slope limiter or artificial dissipation was attempted earlier[6]. We think this approach to be useful and more convenient to use in case of DG methods and further explore its use in viscous and thermo-chemical nonequilibrium hypersonic flows. It is well known that p = 0 (first order accurate method) is sufficient to capture shock of any strength, so using an effective shock indicator technique we can use $p = 0$ in shock regions and higher order polynomial accuracy ($p \geq 1$) in smooth flow regions. We can focus on reducing mesh size in shock and increasing order of accuracy in smooth flow regime to increase over all accuracy of solution. These ideas will be presented in more extensive details in a future publication and are only briefly presented in this paper.

Recent work on DG[7] has demonstrated that sub-cell shock capturing (capturing the shock within an element using artificial dissipation and shock sensor) lacks robustness and may not be more accurate than super-cell shock capturing or refinement (capturing the shock within few elements of reduced size for more accurate shock capturing). We also look into shock refinement option rather than shock capturing for high order DG method. We employ p-adaptivity to use $p = 0$ for shock region and $p \geq 1$ for smooth flow. For refining mesh near shock, rather than going for h-adaptation, we choose r-adaptation in order to just refine cells near shock only, and studying how can we do this more efficiently for hypersonic flow over any general body shape with special interest for problems with detached shock. In this work, we validate steady state solutions, though for thermal ablation, it's essential to obtain a time accurate solution response. Our implicit time scheme is first order accurate. We present validation of our results for inviscid, viscous and thermo-chemical non-equilibrium hypersonic flow problems. Here, we present results for $p = 0$ and 1.

For this work, we also implemented parallelization of MIG[12, 16] (our in-house code) using HYPRE[17]. In our attempts to parallelize the code we are able to achieve speedups of 11 and 22 with two different parallel solvers in HYPRE, namely Euclid preconditioned GMRES and DS preconditioned BiCGStab.

II. Governing Equations

In this section we present governing equations for all the cases presented in the Results and Discussion section. For inviscid and viscous hypersonic flows, we use 2-D Euler and Navier Stokes equations. For Euler equations, we use inviscid flux terms (F_x, F_y) only and for Navier-Stokes equations, we use both inviscid (F_x, F_y) and viscous (F_{vx}, F_{vy}) flux terms presented below,

$$U = \begin{Bmatrix} \rho \\ \rho u \\ \rho v \\ \rho E \end{Bmatrix}, F_x = \begin{Bmatrix} \rho u \\ \rho u^2 + P \\ \rho uv \\ u\left(\rho E + P\right) \end{Bmatrix}, F_y = \begin{Bmatrix} \rho v \\ \rho uv \\ \rho v^2 + P \\ v\left(\rho E + P\right) \end{Bmatrix},$$

$$F_{vx} = \begin{Bmatrix} 0 \\ \tau_{xx} \\ \tau_{xy} \\ u\tau_{xx} + v\tau_{xy} - q_x^{"} \end{Bmatrix}, F_{vy} = \begin{Bmatrix} 0 \\ \tau_{yx} \\ \tau_{yy} \\ u\tau_{yx} + v\tau_{yy} - q_y^{"} \end{Bmatrix} \quad (1)$$

The flux terms will combine in the following form,

$$\frac{\partial U}{\partial t} + \frac{\partial F_x}{\partial x} + \frac{\partial F_y}{\partial y} + \frac{\partial F_{vx}}{\partial x} + \frac{\partial F_{vy}}{\partial y} = 0 \quad (2)$$

In above formulation, viscosity is evaluated from Sutherland's law. For hypersonic flows in thermo-chemical non equilibrium, we use equation in above form (Eq. 2), but we also add a source term, S to Eq. (2) on right hand side. Solution vector, U and inviscid and viscous flux terms, F and F_v are given as follows,

$$U = \begin{Bmatrix} \rho_s \\ \rho_s u \\ \rho_s v \\ \rho e_t \\ \rho e_v \end{Bmatrix}, F_x = \begin{Bmatrix} \rho_s u \\ \rho u^2 + P \\ \rho uv \\ \rho u h_t \\ \rho u e_v \end{Bmatrix}, F_y = \begin{Bmatrix} \rho_s v \\ \rho uv \\ \rho v^2 + P \\ \rho v h_t \\ \rho v e_v \end{Bmatrix},$$

$$F_{vx} = \begin{Bmatrix} \\ -\rho_s \tilde{V}_{sx} \\ \tau_{xx} \\ \tau_{xy} \\ u\tau_{xx} + v\tau_{xy} - q_x^{"} - q_{vx}^{"} - \sum_s h_{t,s}\rho_s \tilde{V}_{sx} \\ -\sum_s e_{v,s}\rho_s \tilde{V}_{sx} - q_{vx}^{"} \end{Bmatrix}, F_{vy} = \begin{Bmatrix} \\ -\rho_s \tilde{V}_{sy} \\ \tau_{yx} \\ \tau_{yy} \\ u\tau_{yx} + v\tau_{yy} - q_y^{"} - q_{vy}^{"} - \sum_s h_{t,s}\rho_s \tilde{V}_{sy} \\ -\sum_s e_{v,s}\rho_s \tilde{V}_{sy} - q_{vy}^{"} \end{Bmatrix} \quad (3)$$

In above equations, ρ_s stands for species density and we consider a total of 5 species, N_2, O_2, NO, N and O. The total and vibrational energies are ρe_t and ρe_v respectively[18]. Total energy includes all the modes of energy transfer, i.e., translational, rotational, vibrational and electronic modes. Vibrational energy however includes vibrational and electronic modes only. Translational and rotational modes are assumed to be at equilibrium with each other at a temperature, T and vibrational and electronic modes are in equilibrium with each at a temperature, T_v. Total mixture density, ρ is given by following,

$$\rho = \sum_s \rho_s \quad (4)$$

The total specific enthalpy, h_t and total species specific enthalpy, $h_{t,s}$ are given by,

$$h_t = e_t + \frac{P}{\rho}$$

$$h_{t,s} = e_{t,s} + \frac{P_s}{\rho_s} = C_{vs}T + e_{v,s} + h_s^0 + \frac{P_s}{\rho_s} \quad (5)$$

Above h_s^0 and P_s are formation enthalpy and partial pressure respectively of species, s, while $C_{vs}T$ and e_{vs} refer to translational-rotational and vibrational-electronic energy modes, respectively. Heat flux terms are given by,

$$q^{"} = -(k_t + k_r)\nabla T$$
$$q_v^{"} = -k_v \nabla T_v \quad (6)$$

For, mass diffusion term, $\rho_s \tilde{V}_s$, Fick's law is used. The mixture viscosity, μ and the thermal conductivity, k are determined from species viscosities and thermal conductivities using Wilke's semi empirical mixing rule and species viscosities are determined from Blottner's curve. The source term for Eq. (2) is given as follows,

$$S = \begin{Bmatrix} \omega_s \\ 0 \\ 0 \\ 0 \\ \sum_s \omega_s e_{v,s} + Q_{TV} \end{Bmatrix} \quad (7)$$

We consider 5 chemical reactions, of which, first three are third body reactions for dissociation of N_2, O_2 and NO. In these reactions, M can be any of the 5 species present, hence we have in total 15 reactions for first three reactions considered. Adding remaining two Zeldovich exchange reactions we get total 17 chemical reactions. These reactions are,

$N_2 + M \leftrightarrow 2N + M$, $O_2 + M \leftrightarrow 2O + M$, $NO + M \leftrightarrow N + O + M$, $N_2 + O \leftrightarrow NO + N$, $NO + N \leftrightarrow O_2 + N$

Zeldovich exchange reactions are responsible for generation of NO. Reaction rates are based on Park's model and values of all coefficients are taken from Ref. 21. The above reactions are endothermic in forward direction. Q_{TV} denotes exchange of energy between translational-rotational and vibrational modes only for polyatomic species, and is evaluated from Landau-Teller model.

III. Numerical Scheme

A. Time-Implicit Backward Euler Discontinuous Galerkin method (2-D framework)

We use our in-house modular finite element based Multiscale Ionized Gas (MIG) flow code for the DG method. This code was also parallelized for domain decomposition and parallel solver using HYPRE. Weak form of 2-D model problem given by Eq. (8) is given in Eq. (9). Multiplying Eq. (8) by a test function, ϕ and integrating over domain (along with integration by parts for viscous and inviscid flux terms) gives us weak form in Eq. (9).

$$\frac{\partial U}{\partial t} + \nabla . F\left(U\right) - \nabla . F_{\mathrm{v}}\left(U, \nabla U\right) = S \tag{8}$$

$$\int_E \left(\phi \frac{\partial U}{\partial t} \right) d\Omega + \oint_{\partial E} \phi F . \vec{n} d\sigma - \int_E \nabla \phi . F d\Omega - \oint_{\partial E} \phi F_v . \vec{n} d\sigma + \int_E \nabla \phi . F_v d\Omega - \int_E \phi S d\Omega = 0 \tag{9}$$

Basis functions chosen for the above formulation are Jacobi polynomials, and are given in Table 1 below. The expressions of these basis functions were taken from Ref. 11. Here, the coordinates x and y are given for a reference square element, which can be transformed to a general quadrilateral in the physical space using bilinear mapping.

Table 1: Basis functions expressions based on their orders. Here x and y are coordinates for reference geometry being a generalized quadrilateral.

Basis/Order	1	2	3	4
1	1	1	1	1
2		$-1+2x$	$-1+2x$	$-1+2x$
3		$-1+2y$	$-1+2y$	$-1+2y$
4			$1-6x+6x^2$	$1-6x+6x^2$
5			$1-2y-2x+2xy$	$1-2y-2x+4xy$
6			$1-6y-6y^2$	$1-6y-6y^2$
7				$-1+12x-30x^2+20x^3$
8				$-1+2y+6x-12xy-6y^2+12xy^2$
9				$-1+6y-6y^2+2x-12xy+12yx^2$
10				$-1+12y-20y^2+20y^3$

For shock identification, we have used shock indicator[6, 7] given as,

$$s_k = \log_{10}\left(\frac{1}{\left|\partial\Omega_k\right|} \int_{\partial\Omega_k} \left| \frac{\left[P_h\right].\vec{n}}{\left\{P_h\right\}} \right| ds \right) \tag{10}$$

In above, $[P_h]$ denotes the jump in pressure across edges of an element, Ω_k, and $\{P_h\}$ denotes average of pressure across the edge. Threshold values of 0.04, 0.1 and 0.3 are considered for s_k, to see their effect on simulations. s_k greater than or equal to threshold value is considered shock region and we apply $p = 0$ over there and in the other regions (i.e. smooth regions) we use $p \geq 1$. For refining the mesh in the shock, we use r-adaptivity, by clustering the elements in the domain outside of the shock to region very close to shock. This can help in avoiding use of large number of mesh elements around the shock.

IV. Results and Discussions

We present results for three cases of hypersonic flow over a circular cylinder. (i) Inviscid flow simulation for a freestream Mach number of 6 (compared with results from Ref. [6]), (ii) Viscous hypersonic flow freestream Mach number of 17 (with results compared from Ref. [7]), and (iii) Flow with thermo-chemical non-equilibrium for freestream Mach number of 17 (results compared with Ref. [18]). These test cases serve as benchmark cases to validate our code for solution capability to solve hypersonic flow problems of varying degree of complexities.

A. Inviscid Hypersonic flow (M = 6) over a circular cylinder (Benchmarked with Ref. [6])

Here we solve for inviscid hypersonic case, using r-p adaptivity. First we simulate the problem with $p = 0$ everywhere to steady state. Then this solution is taken, and by using shock sensor and p-adaptivity method, we apply $p = 1$ solution in regions with smooth flow features and $p = 0$ in regions of shock. The jump indicator based on pressure jump (see above section) values over each edge of the element is used to distinguish between shock and smooth flow regions. This jump indicator is found to be more robust[6, 7] in comparison to the smoothness indicator in Ref. [14]. Also for time accurate simulations, starting from uniform flow as initial solution, when the shock moves along the elements, smoothness indicator fails to provide distinction between regions with $p = 0$ and $p \geq 1$. Shock indicator based on pressure jump doesn't face this issue.

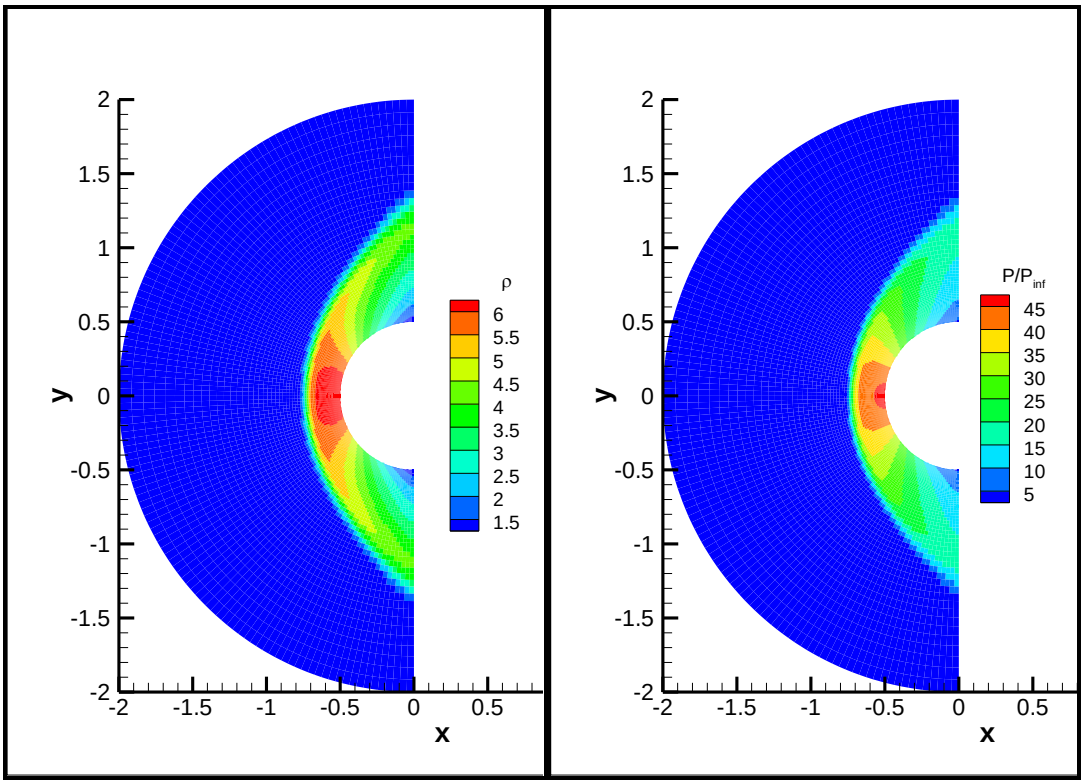

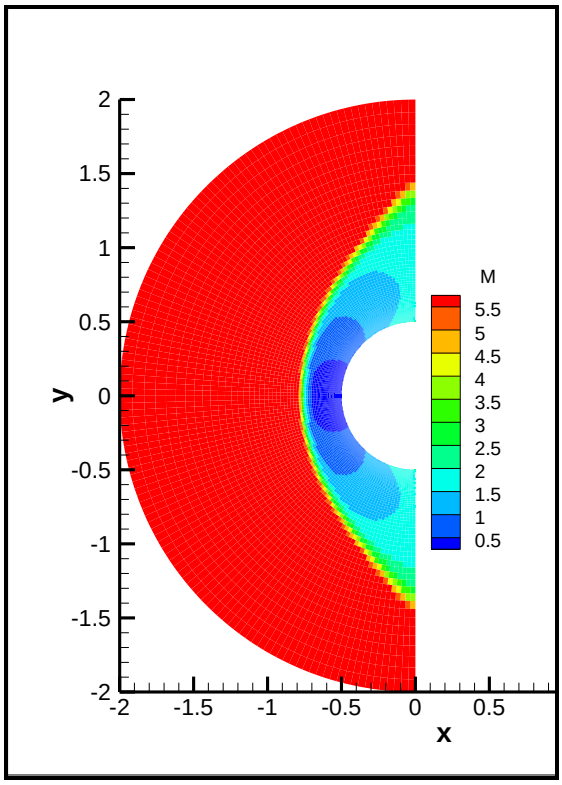

c)

Fig. 1: Inviscid Hypersonic case (p = 0 results). a) Density contours, b) P/P_∞ contours, and c) Mach number contours are shown. Mesh is 128 × 100 elements, 128 in circumferential direction and 100 in radial direction, with finer mesh close to cylinder. Pressure and Mach contours compare well with results published in Ref. [6].

After we obtain a steady state solution with p = 0 and p = 1 using p-adaptivity, we apply r-adaptivity, where using the shock location, we compress the domain bringing it closer to shock. This results in clustering of all the elements on domain outside shock and within shock, close to the shock. The elements can also be clustered in a fashion so that elements closer to shock are finer than elements away from the shock. Thus the shock can be accurately captured, with small mesh elements. This can be repeated several times to get shock's location accurately. After we obtain steady solution on this mesh, we can proceed to p-adaptivity method with p = 2 in smooth flow region and p = 0 in shock regions. This can be extended to higher values of p to increase order of accuracy within smooth region.

In Fig. 1, we show steady state solution obtained with p = 0 for the inviscid hypersonic problem. We show density, pressure (P/P_∞) and Mach number contours. These contours are comparable to the contours given in Ref. [6]. Our next step is to obtain contours with p-adaptivity using p = 1 in regions of shock and p = 0 in smooth flow regions. For this, we take the steady state solution obtained from above figure, using only p = 0 everywhere, and using shock detector based on pressure jump, apply p = 1 in smooth regions and p = 0 in shock regions. Shock location is evaluated at every time step, and p = 0 and p = 1 accordingly applied and the solution is run up to steady state. In Fig. 2 below, density contours along with indicated shock is shown. Density contours are more stretched out in smooth flow regime due to using p = 1 there, but there is also some waviness in the solution near the shock. Reason for waviness is coarse mesh near the shock and higher threshold value used for shock indicator which shows some oscillations. These oscillations persist in solution, although not causing any stability problems. These oscillations in the shock region are shown in 3-D plot of density contours in Fig. 3. We can get rid of oscillations by lowering the shock indicator threshold value (see Fig. 3 b)) or by refining the mesh by redistribution of elements in the rest of the domain outside the shock in close proximity to shock (see Fig. 4), thus reducing mesh size thereof. We don't see oscillations in Fig. 3 b), but then the region of p = 0 is very wide and includes regions from top and bottom of cylinder as well in addition to shock. This may not be useful since we will have poor accuracy in regions above and below shock. Shock indicator which exactly identifies shock and not other regions without shock, will be useful. For this purpose value of 0.1 was seen to best serve the purpose with least oscillations for this particular mesh.

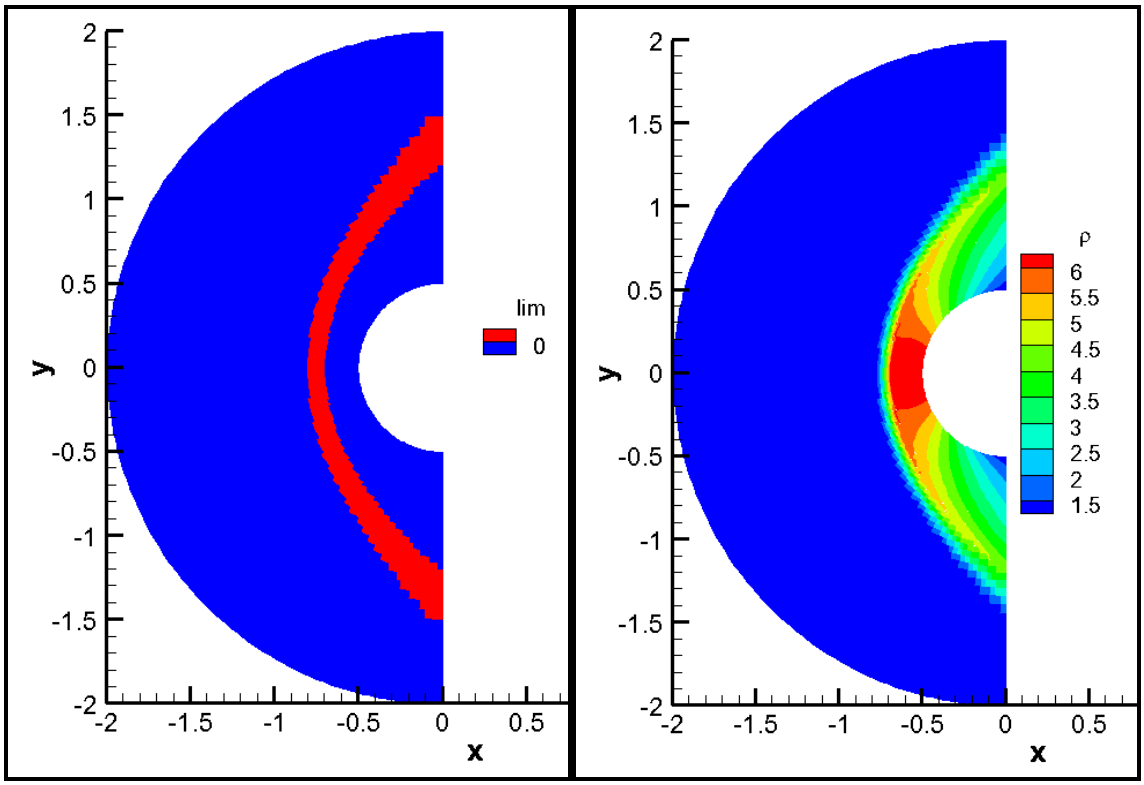

a) b)

Fig. 2: (a) shows shock location as indicated from pressure jump shock indicator. Threshold value of 0.3 is used for the shock indicator. Red region indicates shock (p = 0 is used by setting the limiter to a value of 1) and blue region indicates smooth region, (p = 1 is used by setting limiter to a value of 0). (b) shows density contours with contour levels set same as those with only p = 0. Density contours are more stretched out here in comparison to p = 0, but we can see some waviness in solution near shock.

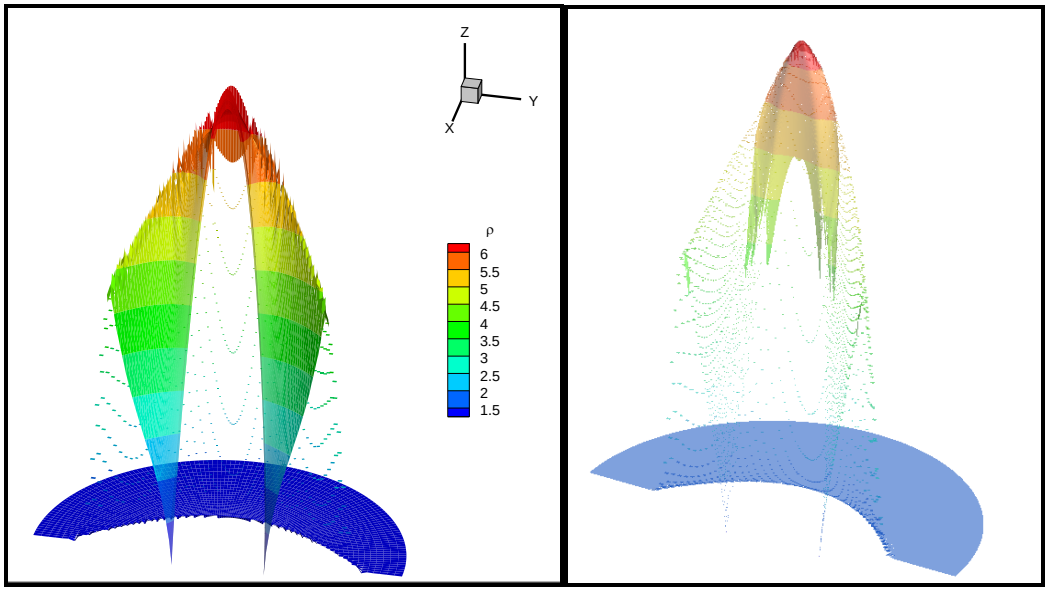

a) b)

Fig. 4: Density contour plots in 3-D with shock indicator threshold values of a) 0.3 and b) 0.04. Decreasing threshold value removes oscillations, but it doesn't much serve the purpose for having high order approximation in the smooth region.

For finer shock resolution, we applied *r-p* adaptivity, bringing the domain elements close to shock region as shown in Fig. 5 a) and b). All the domain elements outside the shock are clustered into the shock uniformly. Thus as we can see the mesh in Fig. 5 a) and b), we get finer elements within the shock region. Contours for pressure, density, Mach number and shock location are shown in Fig. 5 c) – f). It is clearly seen that shock thickness has reduced as compared to above shown results. We still observe some waviness in solution profiles. These solutions haven't yet reached steady state (from the residual perspective; shock's location is stationary). Solution seems to have effect of error wave propagation from shock to the flow in the shock layer, which can be very easily seen in contour plots of Mach number and density. This error wave may be due to difference in accuracy of scheme in shock with $p = 0$ and shock layer with $p = 1$. In these simulations, shock location is being evaluated at every time step, and thus this may cause delay for solution reaching steady state from residual perspective. It will be of interest to find out if the error waves go away when solution reaches steady state, or is it dependent on oscillations near shock which are controlled by adjusting threshold value for shock indicator and also by refining the shock region more and more. Another problem that we note in Fig. 5 is that outside domain is jagged, and this may amplify the wavy nature of solution. So, next step for inviscid simulation will be in direction to resolve all these issues to investigate if we can get accurate solution without all problems that we see below. These steps and the questions are summarized below,

- Getting steady state solution (Do we get reduction or elimination of error waves in solution?)
- Adjusting threshold value of shock indicator (Do oscillations near shock go away?)
- Finer mesh at shock (Does this affect solution or oscillations are reduced due to this?)
- Smoothing of solution domain (How does this affect solution process?)

Assessment of these steps is important for ascertaining a solution for further stages.

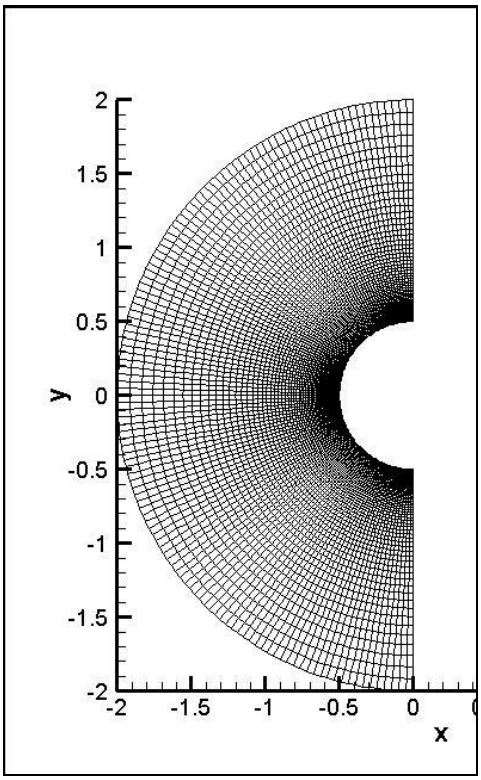

a)

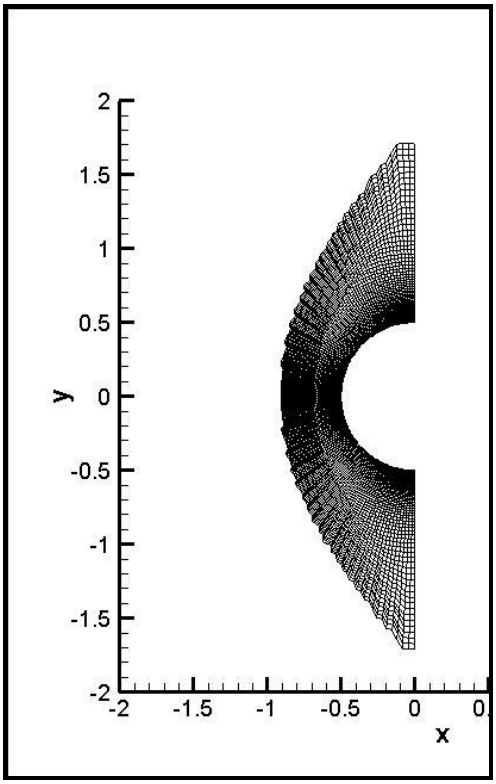

b)

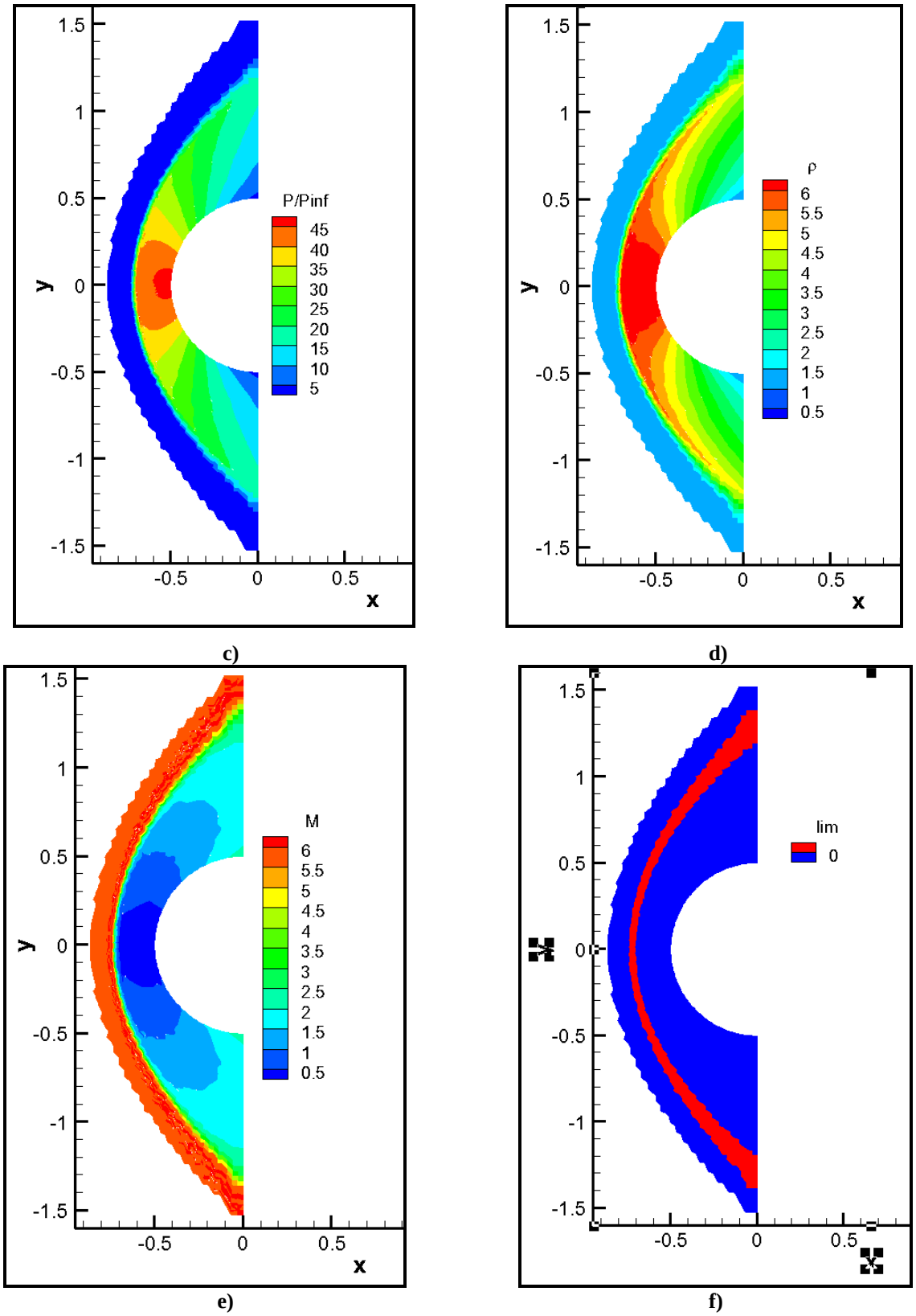

c) d) e) f)

Fig. 5: Contour plots with r-p adaptivity applied with $p = 0$ and $p = 1$. Shock thickness is seen to have reduced. By adjusting the thickness of mesh elements within shock region, shock can be refined to a better extent. However some waviness in solution is still seen, and this may be due to several reasons highlighted above.

B. Viscous Hypersonic flow (M = 17) over a circular cylinder (Benchmarked with Ref. [7])

For hypersonic viscous flow, we used BR1[19] and BR2[20] schemes to model the numerical flux for the viscous term. Advantage of BR2 scheme is that it avoids use of auxiliary variables; hence it's less computationally expensive. According to the literature[22, 23], BR2 scheme is also proven to be more stable than BR1 scheme, though it is derived from BR1 scheme itself. To match the result of hypersonic flow over cylinder for viscous case to the results in literature, we found that the results for $p = 0$ case are very much dependent on the mesh and boundary condition. The sharp gradient of temperature near the wall, as shown in Ref. [7], is not captured with $p = 0$, for a coarse mesh.

The shock stand-off distance in plots below is close to 0.6 m, as opposed to 0.4 m reported results for M=17 flow over cylinder (using perfect gas Navier-Stokes model). This may be related to two boundary conditions that we are using, to $p = 0$ for being dependent on a fine mesh close to wall. At cylinder wall, we enforce no slip condition and a fixed wall temperature of 500 K. For wall boundary, we enforce same pressure as in the flow just next to the wall. Since, same pressure is used, and temperature in flow goes from hot to cold wall temperature, we can apply ideal gas law and predict density at wall. Let's call this Boundary Condition 1 or BC1. We can also use flow density just next to wall for wall density. Let's call this Boundary Condition 2 or BC2. BC1 results in larger density at wall in steady state solution, and shows higher shock standoff distance, as is seen in above simulations and BC2 results in smaller density compared to BC1, and therefore a smaller shock standoff distance. Below we show result obtained with smaller shock standoff distance,

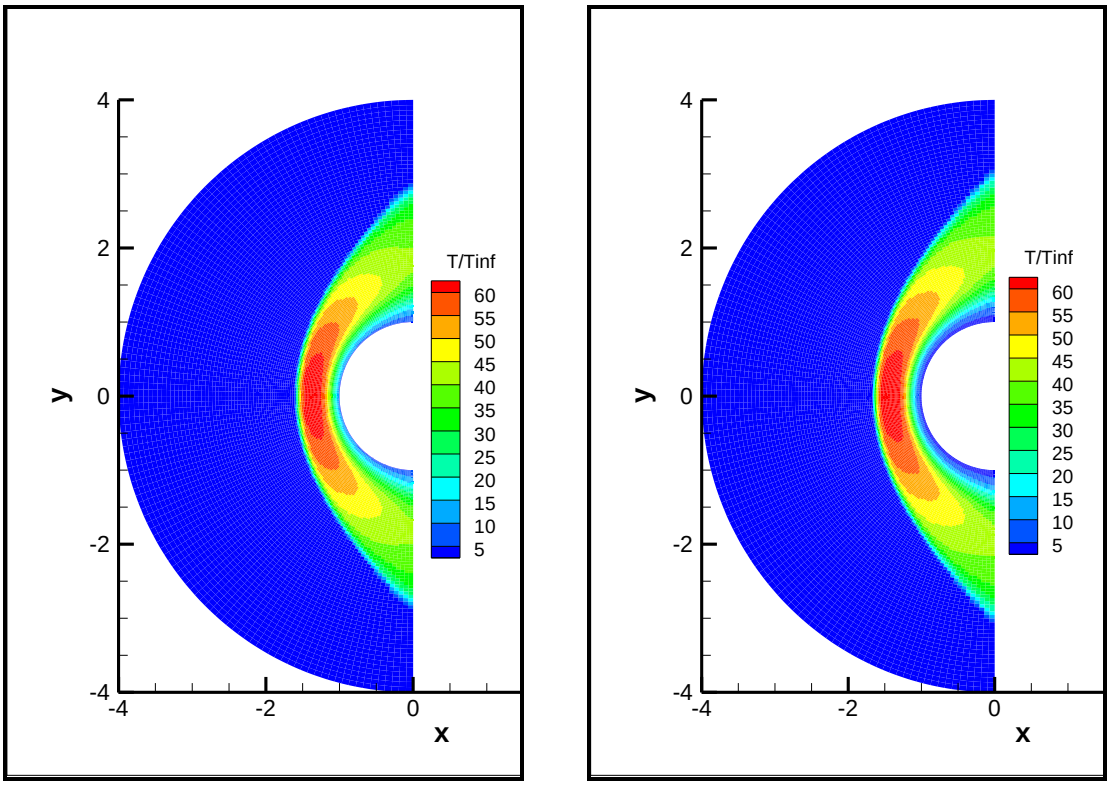

Fig. 6: Contours plot of T/T_∞ for a) BR2 scheme and b) BR1 scheme. Mesh in a) has a thickness of 0.001 m near wall and in b) a thickness of 0.01 m thickness near wall. Shock standoff distance in a) is 0.53 m and in b) is 0.65 m, as opposed to published result[7] of 0.4 m. This is attributed to two types of boundary condition used, coarseness of mesh near wall and $p = 0$.

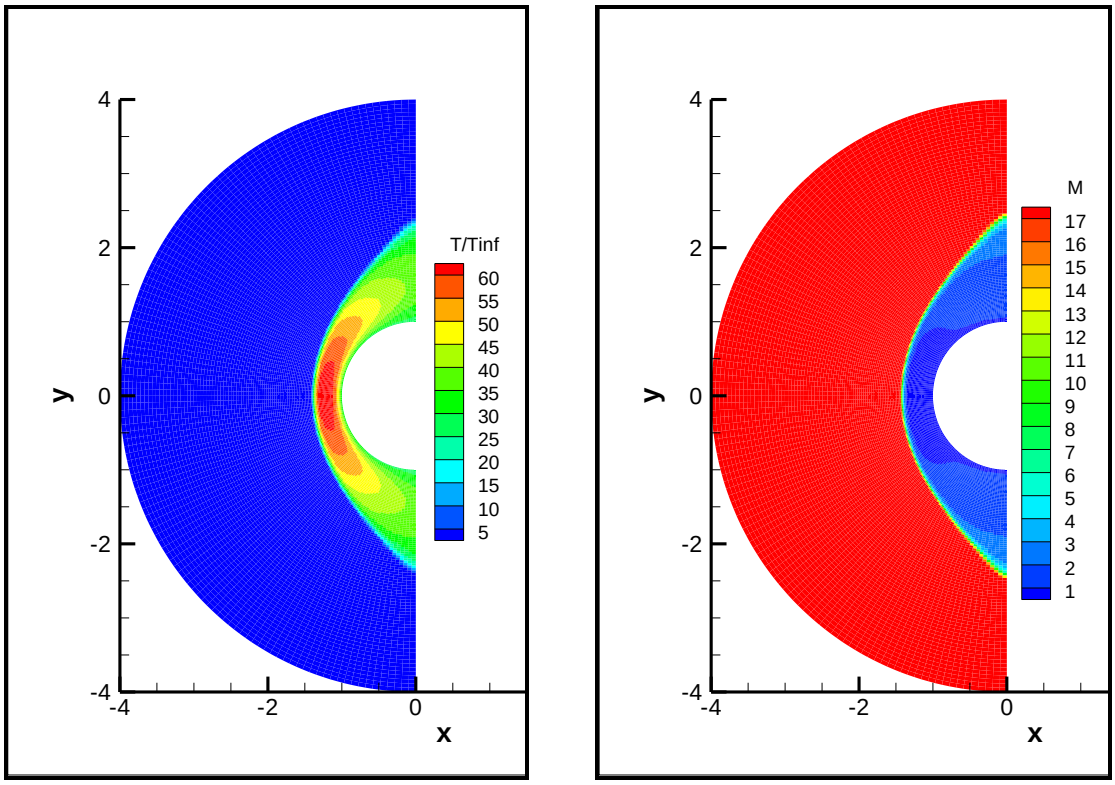

a) b)

Fig. 7: Above is a simulation with BC2, and mesh thickness of 0.01 m near wall, and shows shock standoff distance of 0.35 m. b) shows Mach contours which are also not aligned with that shown in published literature. These results will be resolved for p = 1 and 2.

A shock indicator was used in this case to identify regions of shock, and p = 1 was used in smooth regions and p = 0 in shock regions, as in above inviscid case. However in beginning mesh, we used mesh spacing of 0.01 m next to the wall. This was insufficient to capture boundary gradients with sufficient mesh resolution.

C. Thermo-chemical non-equilibrium hypersonic flow (M = 17) over a circular cylinder (Benchmarked with Ref. [18])

In this section, we present results for hypersonic flow with thermo-chemical non-equilibrium for a Mach 17 flow over cylinder. In this case, wall is considered to be super-catalytic and isothermal at temperature of 500 K. Super-catalytic boundary condition implies all species will recombine to give freestream species. The exact initial conditions are T_∞ = 200 K, $T_{v\infty}$ = 200 K, ρ_∞ = 0.001 kg/m^3, u_∞ = 5000 m/s, v_∞ = 0 m/s. Freestream gas is air and therefore individual densities of N_2 and O_2 are 0.7562e-3 Kg/m^3 and 0.2438e-3 Kg/m^3 respectively.

For comparison, we attempt to match our results with Ref. [18]. In Fig. 8, we notice that the shock standoff distance is 0.125 m as compared to 0.2 m in Ref. [18]. Temperature predicted in these simulations is very low (3500 K) in comparison to viscous simulations (12000 K) presented above. We predict T_{max} = 3450 K, and T_{vmax} = 3200 K. In published results, T and T_v in majority of domain is 5200 K, and T_{max} = 7700 K and T_{vmax} = 5700 K. We also present a comparison of temperature plot on stagnation line in front of cylinder. It is to be noted that the coefficients of chemical reactions were taken from Ref. [21] and are not exactly same as Ref. [18]. Chemical reactions are all endothermic in forward direction, and hence it seems from the results that forward direction has been prominent, and thus leads to a decrease in total temperature, which may be the reason for observing lower temperatures within the domain. We will test out the code with chemistry rates from Ref. [18].

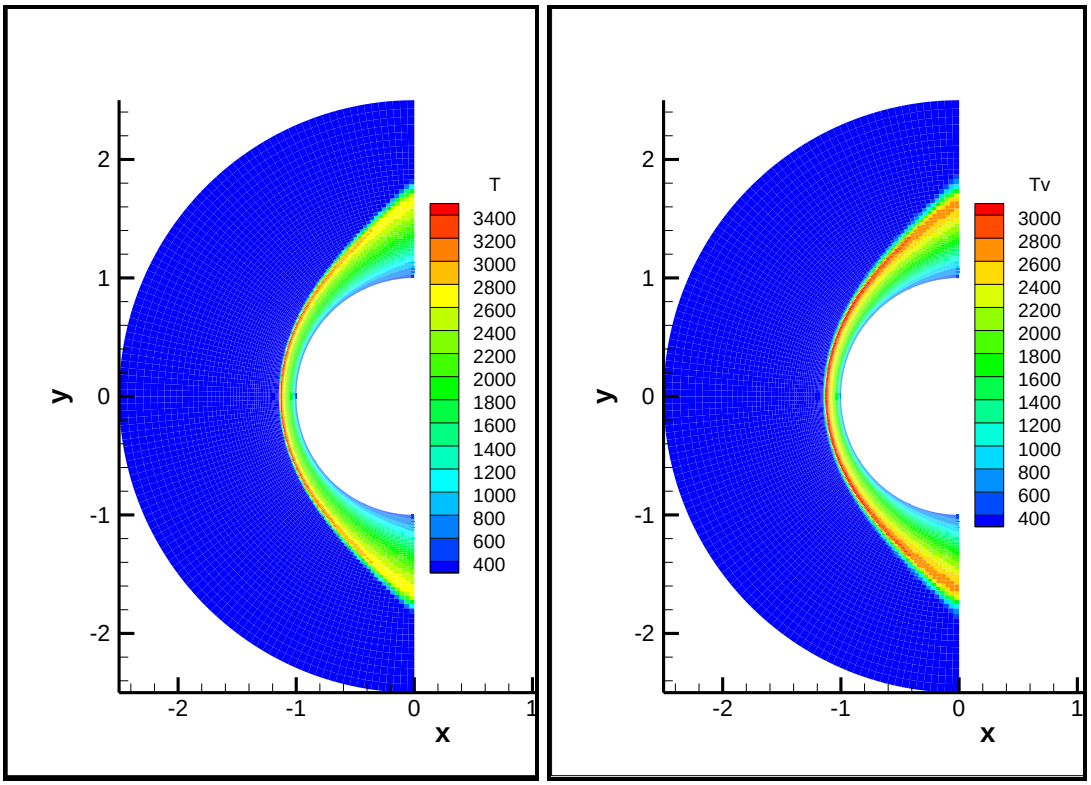

a) **b)**

Fig. 8: Contour plots of a) translational-rotational temperature, T and b) vibrational temperature, T_v, at steady state. Maximum value of T is 3450 K and T_v is 3200 K, which is smaller compared to values presented in Ref. [18]. Shock standoff distance is 0.125 m as compared to 0.2 m in Ref. [18]. Reason for this may be different rates of chemical reactions used from Ref. [21], which is not the same as of Ref. [18]. It seems that the chemistry is dominant in forward direction, which is endothermic and hence lowers the temperature much more than what we expect. Rates of coefficients of chemical reactions are being investigated.

Pressure and Mach contours are also shown in Fig. 9. In comparison to viscous flow simulations above, pressure contours are similar shape and same magnitude, but shock standoff distance is lower. This is due to the fact that chemical reactions can change temperature in the shock and shock layer and hence alter shock standoff distance.

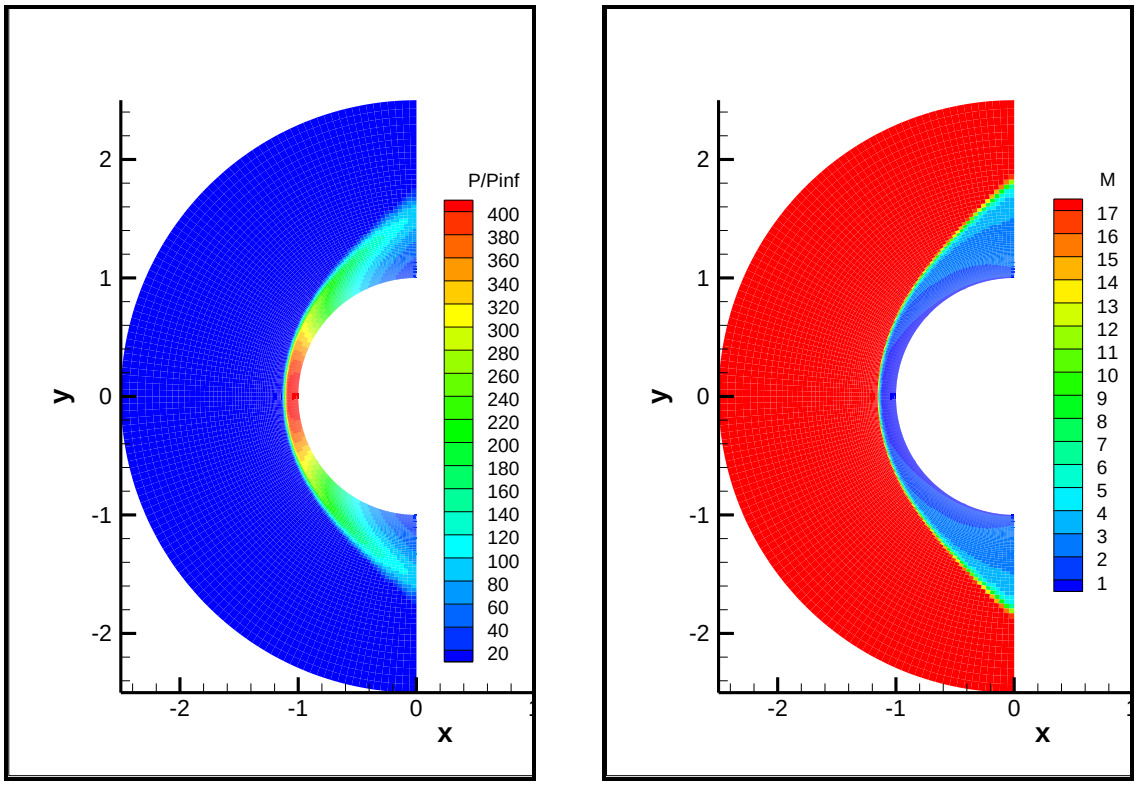

a) b)

Fig. 9: Pressure and Mach contours for hypersonic flow with thermo-chemical non-equilibrium.

Now we will discuss chemistry of this simulation, first we show forward reaction rates vs. T, as given in Ref. [21] and Ref. [18].

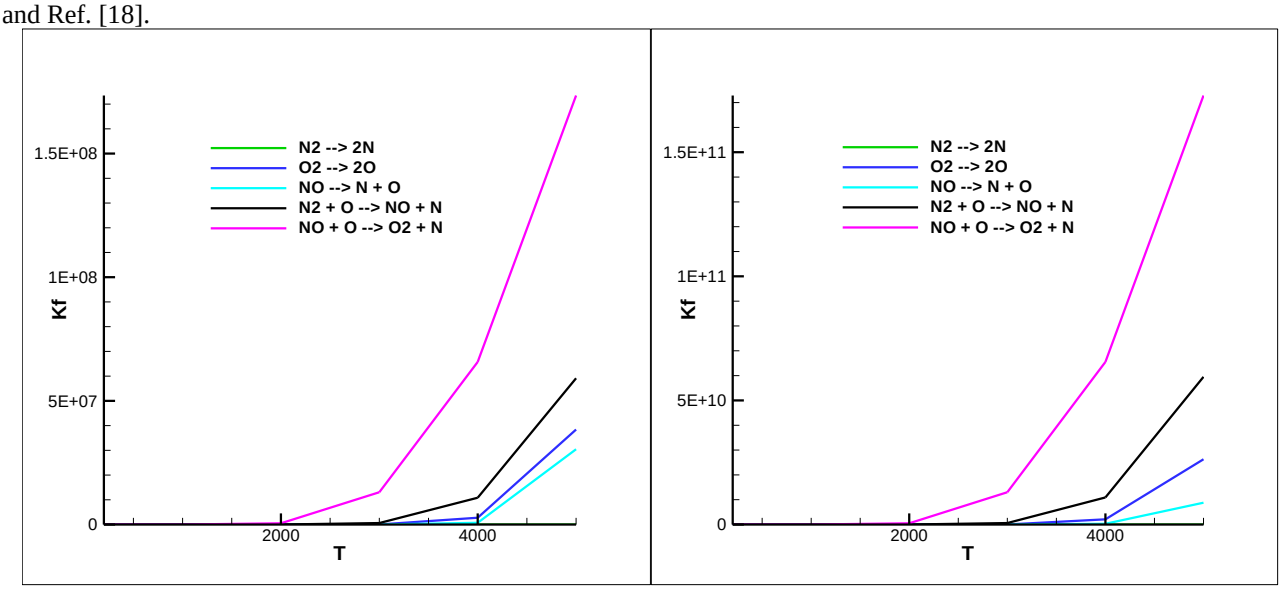

a) b)

Fig. 10: Plots for forward reaction coefficient given in a) Nompelis[21] and b) Lockwood[18] with temperature, *T*. This shows N_2 dissociation is weakest of all chemical reactions and last two chemical reactions have highest reaction rates.

Below we show contours of mass fraction of each species. From chemistry plots that we see below, we see mass fractions of each species present in domain in steady state solution. This can help us understand why we have such a low

temperature in domain. It can be seen that O_2 dissociates into O in the shock, and the produced atomic oxygen reacts with resent N_2 to form NO and N. This NO then reacts with O again to form O_2 and N. Thus we see that O_2 reduces only a little in the shock, as O_2 kept in balance by first and last reaction. NO produced by 4^{th} reaction is used by 5^{th} reaction to form N, and thus we see higher mass fraction of N as compared to NO within the shock layer. Mass fraction of NO peaks just after the shock, whereas mass fraction of N peaks within the shock layer. O_2 doesn't get totally reduced in the shock region, as we might expect, since it is balanced by last reaction. Reaction rates of O_2 dissociation (see above figures) given in two references, do not differ significantly. Fifth reaction, i.e. exchange of O with NO to form O_2, is the strongest of all reactions, and thus governs that O_2 will not totally diminish in the shock region. Fourth and fifth reactions also have the highest reaction rates in the forward direction for concerned temperatures, and they lead to high formation of N within the domain. Fourth reaction is the main source of N since N_2 is sufficiently present. Dissociation of N_2 is weakest of all reactions and hence this reaction cannot be considered the main source of N. Since reactions mainly happen in forward direction, which is endothermic, we surmise this to be the reason for lower temperature prediction.

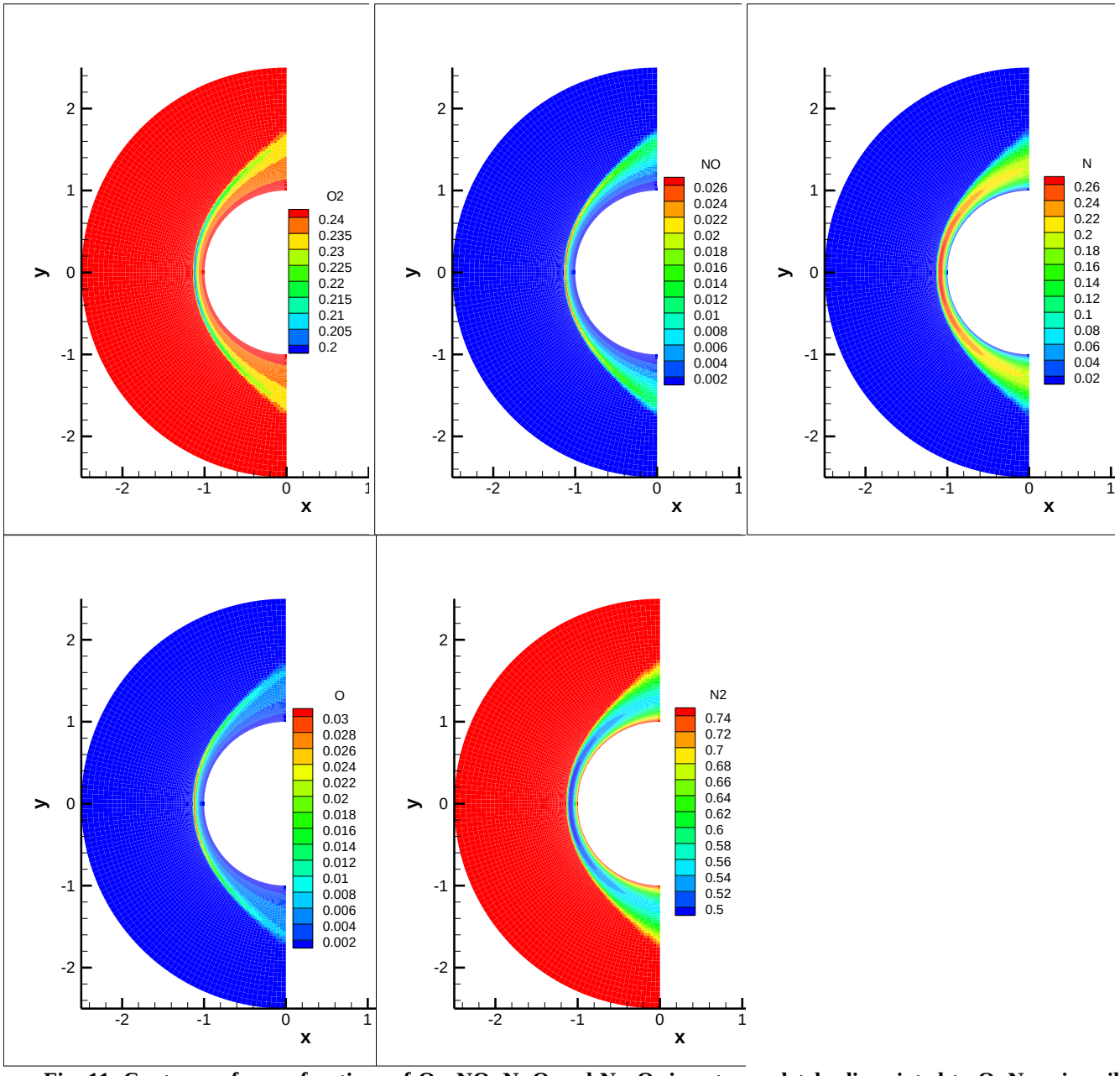

Fig. 11. Contours of mass fractions of O_2, NO, N, O and N_2. O_2 is not completely dissociated to O. N_2 primarily reduces to N through last two reactions.

V. Conclusion

We have proposed *r-p* adaptivity as an alternative to *h-p* adaptive scheme to avoid use of excessive elements to capture shock through shock refinement procedure. The *p*-adaptivity also allows us to capture shocks without using any slope limiters or artificial dissipation in the scheme and this is demonstrated for both inviscid and viscous hypersonic flows. Inviscid results with $p = 1$ have some waviness in solution, which also doesn't allow solution to reach steady state. More work remains in both inviscid and viscous cases to finalize the working of this scheme. Preliminary results with $p = 0$ are shown for thermo-chemical non-equilibrium flows, and reason for discrepancy in shock standoff distance and lower temperatures is being investigated. We are currently working with $p = 1$ case for the viscous code for validation. All the cases will also be implemented for quadratic polynomial approximation, i.e. $p = 2$, and possible benefits of using r-p adaptive approach in general for hypersonic flows, over h-p adaptive scheme will be explored in future work.

Acknowledgments

This work is partially funded by the AFRL Contract (through UES, Inc.) The authors acknowledge Dr. Ryan Gosse from Air Force Research Laboratory for his insightful research input.

References

[1]B. Cockburn, C.-W.Shu, "TVB Runge-Kutta local projection discontinuous Galerkin finite element method for conservation laws V: Multidimensional systems", *J. Comput. Phys.*, 141:199-224, 1998.

[2]F. Bassi, S. Rebay, "A high order accurate discontinuous finite element method for the numerical solution of compressible Navier-Stokes equation", *J. Comput. Phys.*, 131(2), 1997.

[3]P.-O. Persson, J. Peraire, "Newton-GMRES preconditioning for Discontinuous Galerkin Discretizations of the Navier-Stokes Equations", *SIAM J. Sci. Comput.*, Vol. 30, No. 6, pp. 2709-2733, 2008.

[4]N.C. Nguyen, P.-O. Persson, J. Peraire, "RANS Solutions Using High Order Discontinuous Galerkin Methods", *Proc. of the 45th AIAA Aerospace Sciences Meeting and Exhibit*, AIAA-2007-914, January 2007.

[5]P. Houston, D. Schoetzau, X. Wei, "A Mixed Discontinuous Galerkin Method for Incompressible Magnetohydrodynamics", *Journal of Scientific Computing*, 2008.

[6]Li Wang, "Techniques for High-Order Adaptive Discontinuous Galerkin Discretizations in Fluid Dynamics", Ph. D. Thesis, University of Wyoming, April 2009.

[7]Nick Burgess, "An Adaptive Discontinuous Galerkin Solver for Aerodynamic Flows", Ph. D. Thesis, University of Wyoming, November 2011.

[8]C. R. Nastase, D. J. Mavriplis, "A parallel hp-multigrid solver for three-dimensional discontinuous Galerkin discretizations of the Euler equations", AIAA Paper 2007-0512, January 2007.

[9]C. R. Nastase, D. J. Mavriplis, "High-order discontinuous Galerkin methods using an hp-multigrid approach", J. Comput. Phys. 213 (1) (2006) 330–357.

[10]P.-O. Persson, J. Peraire, An efficient low memory implicit DG algorithm for time dependent problems", AIAA Paper 2006-112, January 2006.

[11]B. Landmann, "A parallel discontinuous Galerkin code for the Navier-Stokes and Reynolds-averaged Navier-Stokes equations", *Ph.D. thesis*,University of Stuttgart, Germany, 2008.

[12]A. Bhatia, S. Roy and R. Gosse, "Pyrolysis gas flow in thermally ablating media using time implicit discontinuous Galerkin method", AIAA 2011-145, *49th AIAA Aerospace Sciences Meeting including the New Horizons Forum and Aerospace Exposition*, 4 - 7 January 2011, Orlando, Florida.

[13]Douglas J. Quattrochi, "Hypersonic Heat Transfer and Anisotropic Visualization with a Higher Order Discontinuous Galerkin Finite Element Method", M. S. Thesis, Massachusetts Institute of Technology, June 2006.

[14]P.-O. Persson J. Peraire, "Sub-cell shock capturing for discontinuous Galerkin methods", In Proceedings of 44th Aerospace Sciences Meeting and Exhibit, Reno NV, AIAA Paper 2006-112, Jan 2006.

[15]B. Cockburn, S. Hou, and C.-W. Shu, "The Runge-Kutta local projection discontinuous Galerkin finite element method for conservation laws IV: The multidimensional case", Math. Comput., 54(545), 1990.

[16]A. Bhatia, S. Roy, "Modeling the motion of pyrolysis gas through the charring ablating material using discontinuous Galerkin method", *AIAA 2010-982, 48th AIAA Aerospace Sciences Meeting Including the New Horizons Forum and Aerospace Exposition*, 4 - 7 January 2010, Orlando, Florida.

[17]R. Falgout et al., "HYPRE high performance preconditioners", Users Manual, *Center for Applied Scientific Computing, Lawrence Livermore National Laboratory*, Software version: 2.7.0b

[18]Brian A. Lockwood, "Gradient-Based Approaches for Sensitivity Analysis and Uncertainty Quantification within Hypersonic Flows", Ph. D. Thesis, University of Wyoming, May 2012.

[19]F. Bassi, S. Rebay, "A high-order accurate discontinuous finite element method for the numerical solution of the compressible Navier{Stokes equations", Journal of Computational Physics, 131(2), 1997.

[20]F. Bassi and S. Rebay, "Discontinuous Galerkin solution of the Reynolds-averaged Navier-Stokes and k-ω turbulence model equations", Journal of Computers & Fluids, 34:507-540, 2005.

[21]Ioannis Nompelis, "Computational Study of Hypersonic Double-Cone Experiments for Code Validation", Ph. D. Thesis, University of Minnesota, May 2004.

[22]D. N. Arnold, F. Brezzi, B. Cockburn, and D. Marini, "Discontinuous Galerkin methods for elliptic problems", In B. Cockburn, G. E. Karniadakis, and C.-W. Shu, editors, Discontinuous Galerkin Methods, volume 11 of LNCSE, pages 89-101. Springer, 2000.

[23]D. N. Arnold, F. Brezzi, B. Cockburn, and D. Marini, "Unified analysis of discontinuous Galerkin methods for elliptic problems", SIAM J. Numer. Anal., 39(5):1749-1779, 2001.